Geoscientific
Model Development
Discussions

Open Access

EGU

A preliminary evaluation of WRF (ARW v4.1.1)/DART (Manhattan release v9.8.0)-RTTOV (v12.3) in assimilating satellite visible radiance data for a cyclone case

Yongbo Zhou[1,2], Yubao Liu[1,2], Zhaoyang Huo[1,2], Yang Li[1,2]

5 [1]School of Atmospheric Physics, Nanjing University of Information Science and Technology, Nanjing, China

[2]Precision Regional Earth Modeling and Information Center (PREMIC), Nanjing University of Information Science and Technology, Nanjing, China

Correspondence to: Yongbo Zhou (yongbo.zhou@nuist.edu.cn)

Abstract. Satellite visible (VIS) radiance data contain rich cloud information that are increasingly assimilated for improving
10 cloud and precipitation forecasting of numerical weather prediction models. Recently, the Data Assimilation Research Testbed (DART), a widely used data assimilation resource that supports the Weather Research and Forecasting (WRF) model, was facilitated with an interface for the Radiative Transfer for TOVS (RTTOV), which supports radiance assimilation from visible (VIS) to microwave wavelength channels. This study evaluates the WRF (ARW v4.1.1)/DART (Manhattan release v9.8.0)-RTTOV (v12.3) system for assimilating the radiance data of channel 2 (0.55 ~ 0.75 μm) of the Advanced Geostationary
15 Radiation Imager (AGRI) onboard FY-4. Observing System Simulation Experiments (OSSEs) were performed for a cyclone case. The results indicate that assimilating VIS radiance data improves cloud forecast skills in general. Best results were achieved for the data assimilation (DA) experiment with dense observations and high updating frequency. The best results could capture the "eye" structure of the cyclone system and significantly improves cloud water path and cloud coverage simulations. Nevertheless, three main problems were revealed. The first is its inability to improve cloud vertical distribution
20 such as layered structures and cloud phases; The second is the its inability to influence atmosphere thermodynamic state variables positively; The third is a waste of up to 50% observations during the filtering processes.

Geoscientific
Model Development
Discussions

EGU Open Access

1. Introduction

Satellite data assimilation (DA) has shown great potential to improve weather forecasts (Bauer et al., 2011). Most DA-related
25 studies deal with infrared (IR) and microwave (MW) data, revealing positive effects on cloud and precipitation forecasting by
adjusting the atmospheric state variables such as humidity and temperature (Ma et al., 2017; Geer et al., 2019; Migliorini &
Candy, 2019) as well as cloud-related parameters such as cloud water/ice content and cloud coverage (Zhang et al., 2013;
Yang et al., 2016). To further improve cloud forecasts, there are great potentials in assimilating visible (VIS) and shortwave
infrared (collectively referred to as shortwave, SW) data (Vukicevic et al., 2004; Polkinghorne & Vukicevic, 2011; Scheck et
30 al., 2020; Schröttle et al., 2020) because these measurements contain supplementary and unique cloud information other than
the IR and MW radiance data (Kostka et al., 2014; Schröttle et al., 2020). For example, SW radiation can penetrate a certain
depth of cloud fields, and connotate cloud microphysical properties such as effective particle radius (Re) (Nakajima & King,
1990). In comparison, satellite IR data only provide cloud top microphysics (Xue, 2009). As a complement to weather radar
that is much more sensitive to large hydrometeors or precipitation particles (Keat et al., 2019) usually occurring at the mature
35 and developing stages of convective systems (Zhang and Fu, 2018), satellite SW signals are closely related to small cloud
droplets. Furthermore, SW data usually have higher spatial resolution than IR and MW data (Yang et al., 2017; Coste et al.,
2017; Schimit et al., 2018). Therefore, SW radiance provides higher-resolution cloud properties that are of great significance
for cloud-resolving model simulations.

Many studies have attempted to assimilate the SW radiance data (direct assimilation) rather than the retrieved cloud
40 parameters (indirect assimilation). Direct assimilation critically relies on observation operators. Several observation operators
and relevant algorithms have been developed. For example, in Vukicevic et al. (2004)'s study, model state variables were
mapped to the equivalent radiance by an observation operator for the VIS and IR radiance measurements (VISIROO).
Polkinghorne and Vukicevic (2011) used the Spherical Harmonic Discrete Ordinate Method Plane Parallel for Data
Assimilation (SHDOMPPDA) for radiance conversion. SHDOMPPDA solves radiative transfer processes by discrete ordinate
45 method (DOM) in Cartesian space while computes source functions using spherical harmonic series in spherical space.
Compared with observation operators which solve source functions in Cartesian space, SHDOMPPDA has an advantage of
high computation efficiency. Scheck et al. (2016a) developed a method for fast satellite image synthesis (MFASIS). MFASIS
is a look-up table (LUT)-based observation operator. A comparison study by Scheck et al. (2016b) showed that MFASIS
generates sufficiently accurate results and is 2 ~ 4 orders of magnitude faster than other DOM-based observation operators.
50 Furthermore, a correction method was implemented into MFASIS to reduce errors due to three-dimensional (3D) radiative
effects (Scheck et al., 2018). MFASIS is one of the radiative solvers of the Radiative Transfer for TOVS (RTTOV), one of the
most widely used observation operators in assimilating satellite radiance data. Other radiative transfer solvers of RTTOV
include DOM and single-scattering methods for the SW radiative processes. These solvers could tackle cloud fraction, parallax
correction, and many other critical aspects including molecular absorption and scattering, underlying surface reflection, etc.
55 (Saunders et al., 2018). Apart from these aforementioned observation operators, some machine learning-based observation

Geoscientific
Model Development
Discussions

operators and relevant methods (Scheck, 2021; Zhou et al., 2021) were developed to achieve higher computation efficiency and accuracy for VIS radiance DA.

Nowadays, there are two general approaches for assimilating VIS radiance data. The first approach is the variational (VAR) methods. Vukicevic et al. (2004) assimilated the GOES-9 VIS radiance data to the Regional Atmospheric Modeling

60   System (RAMS) with a four-dimensional VAR (4D-VAR) DA system, exhibiting positive effects on the short-term forecasting of a stratus cloud field. Similarly, Polkinghorne and Vukicevic (2011) assimilated the GOES-8 VIS and IR radiance data to RAMS by a 4D-VAR DA system and indicated that the assimilation can effectively reduce the normalized cost function and the gradient of objective functions with the increase of iteration numbers.

The second approach is the ensemble-based methods. Schröttle et al. (2020) assimilated VIS and IR radiance data in

65   idealized observing system simulation experiments (OSSEs) based on a local ensemble transform Kalman filter (LETKF) approach. Their results indicated that assimilating VIS radiance data alone could improve the forecasting skills of the regional model termed Consortium for Small-scale Modeling (COSMO), and that assimilating the VIS and IR radiance data collaboratively could further improve the forecasting skills. Their findings were validated by Scheck et al. (2020). They concluded that assimilating the VIS radiance data of Spinning Enhanced Visible and Infrared Imager (SEVIRI) on

70   METEOSAT could improve cloud and precipitation forecasts, and, meanwhile, the temperature and water vapour forecasting errors were reduced in most conditions after the DA process.

The VAR and ensemble-based approaches are considered complementary to each other. For example, the ensemble-based approaches generate the flow-dependent background error covariance matrices. On the other hand, the flow-dependence can be used to leverage the VAR approaches. Therefore, several "hybrid" approaches have been developed and great achievements

75   have been made (Kong et al., 2018; Lei et al., 2021).

The ensemble-based methods are remarkably stable for nonlinear systems and are widely used for cloud- and precipitation-related studies (Lei et al., 2015; Kurzrock et al, 2019). Nowadays, there are various community DA resources of the ensemble-based methods, such as the Data Assimilation Research Testbed (DART; Anderson et al., 2009) which supports many numerical models including the Weather Research and Forecasting (WRF) model (Skamarock et al., 2008). Recently,

80   WRF/DART incorporated the RTTOV observation operator, facilitating the assimilation of satellite radiance from VIS to MW wavelengths, enabling it with a great potential in assimilating satellite SW radiance data which are affected by clouds. The Advanced Geostationary Radiation Imager (AGRI) on FY-4 excels at high sampling frequency (5 min for intensive observation and 15 min for usual observation) and high spatial resolution (0.5 ~ 2 km, depending on channels). Zhang et al. (2019) pointed out that AGRI has great application prospects in describing rapidly evolving and small- to medium-scale atmospheric systems.

85   This study explores the potential of WRF/DART-RTTOV system in assimilating the FY-4/AGRI VIS radiance, and evaluates the performance of the system with different observation settings and other model settings, and identifies the limitations. The paper is organized as follows. The models and experiment designs are introduced in Section 2. The results are presented in Sections 3. Discussions on observation rejection are elaborated in Section 4. Conclusions are summarized in Section 5.

2. Models and experiment designs

The performance of the WRF/DART-RTTOV system in assimilating AGRI channel 2 (0.55 ~ 0.75 μm) radiance data were demonstrated with OSSEs. A nature run is performed to generate a proxy true atmosphere for the OSSEs and a control run without DA was performed, provided a baseline for comparison. Impacts of VIS radiance on cloud analysis and forecast were evaluated by designing different DA experiments with the OSSEs framework. Experiments with different observing and updating scenarios were conducted and verified by comparing simulation results with the nature run. The details of the model configuration of the nature run, control run, and experiment runs and the weather case description are provided below.

2.1 Configurations of the WRF Model

The WRF model domain for this study covers parts of the East Asia and Western Pacific (Figure 1). The domain contains 151×177 horizontal grids with a grid spacing of 15 km in the horizontal directions and 40 vertical levels. The model top is set to 50 hPa. To avoid the disturbances over the regions close to the model domain boundaries, simulations within the inner rectangle of 131×157 horizontal grids are analysed.
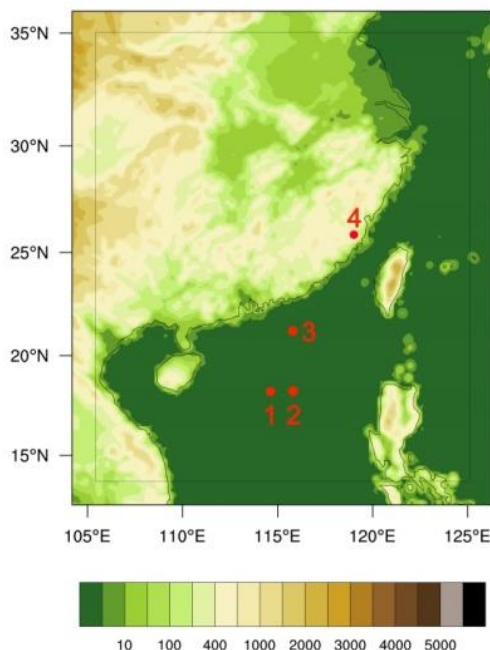
Figure 1. The WRF model domain with 15-km horizontal grid spacing. Only observations within the inner rectangle are assimilated to discard regions close to the model domain boundaries. Red dots denote the points where pointwise-data assimilation experiments were evaluated.

The true state is represented by the ensemble mean of 50 members of the nature run. For each ensemble member of the nature run, the initial conditions (ICs) and lateral boundary conditions (LBCs) were extracted from the National Centers for

Environmental Prediction (NCEP) Final (FNL) Operational Global Analysis data (1 °×1 ° resolution). Perturbations extracted

110   from the WRF 3D-VAR system using a generic background error option which draws the NCEP background error covariances with proper scaling were added to the ICs. The scaling factors for the variance, horizontal length scale, and vertical length scale are set to 0.25, 1.0, and 1.5, respectively. Perturbations of the LBCs are generated based on random variation approach built in the DART *pert_wrf_bc* module. The WRF model configuration includes the "CONUS" physics suite and the NSSL 2-moment microphysical scheme without hail (Mansell et al., 2010). Other model configurations are by default provided by the

115   standard WRF release. The WRF ensemble members are advanced from the perturbed ICs and LBCs at 12:00 UTC 18 August 2020 to 01:00 UTC 19 August 2020.

For the control and DA experiment runs, the ensemble size is set to 50 and the ICs and LBCs were extracted from the ERA5 hourly data (0.25 °×0.25 ° resolution). The WRF model physical parameterization schemes include the WDM6 microphysics scheme (Lim & Hong, 2010), the Betts-Miller-Janjic Cumulus Parameterization option (Betts, 1986; Betts &

120   Miller 1986; Janjić, 1994), the Rapid Radiative Transfer Model for Global Climate Models (RRTMG) longwave and shortwave radiation schemes (Iacono et al., 2008), the GFS planetary boundary layer scheme (Hong and Pan, 1996), the Eta similarity surface layer model (Janjić, 1996), and the Noah Land Surface Model (Ek et al., 2003). The perturbations were added to the LBCs and ICs with the same techniques as the nature run.

2.2 Configurations of RTTOV

125   Synthetic AGRI channel 2 radiance "observations" were simulated by the RTTOV radiative transfer model that was incorporated into the WRF/DART system as a forward operator. For simplicity, the solar zenith angle, solar azimuth angle, satellite viewing zenith angle, and satellite azimuth angle are set to 25.0 °, 75.0 °, 40.0 °, and 210.0 ° during the filtering processes unless otherwisely noted. In addition, an observation error of 1 mW m^{-2} sr^{-1} were assigned during the filtering processes. RTTOV includes the pre-defined cloud optical properties. For liquid water clouds, we use the "Deff" scheme where cloud

130   optical properties are parameterized in terms of Re (Mayer & Kylling, 2005). The cirrus scheme developed by Baren et al. (2014) (hereafter Baren-2014) was used to calculate ice cloud optical properties. It is noted that the Baran-2014 scheme has no explicit dependence on ice particle size. In this study, liquid water particles include cloud water droplets and rain drops, and ice particles include ice, snow, and graupel.

The radiative transfer processes are simulated by the DOM solver in RTTOV. The general radiative transfer options

135   account for atmospheric refraction and curvature. The surface is treated as a specular reflector for downwelling emitted radiance. For land surface, the surface Bidirectional Reflectance Distribution Function (BRDF) were drawn from land surface atlases (Vidot and Borbás, 2014; Vidot et al., 2018). For sea surface, BRDF was calculated by the JONSWAP (Hasselmann et al., 1973) solar sea BRDF model. The lay-to-space transmittance is computed by the v9 predictor on 54 levels (Matricardi, 2008). The downwelling atmospheric emission is computed using the linear-in-tau approximation for the Planck source term.

140   Water vapour profiles were drawn from WRF state variables. Other parameters not explicitly mentioned are by default.

Based on the above model configurations, the dependence of AGRI channel 2 radiance on the liquid water path (LWP), Re, and ice water path (IWP) is presented by Figure 2. The curvature properties clearly show a non-linear relationship between the observations (radiance) and cloud related parameters (LWP, Re, IWP). The differences between the radiance-LWP functions with different effective radii become smaller with as Re increases. For Re larger than 30 μm, the radiance-LWP functions for different effective radii are ignorable. Because raindrops are several orders larger than cloud droplets, the effective radius of cloud droplet is sufficient to describe the radiative transfer processes for the clouds where cloud droplets and raindrops coexist. As a result, Re in the following discussion explicitly denote the effective radius of cloud droplets, which corresponds to the WRF state variable "RE_CLOUD".
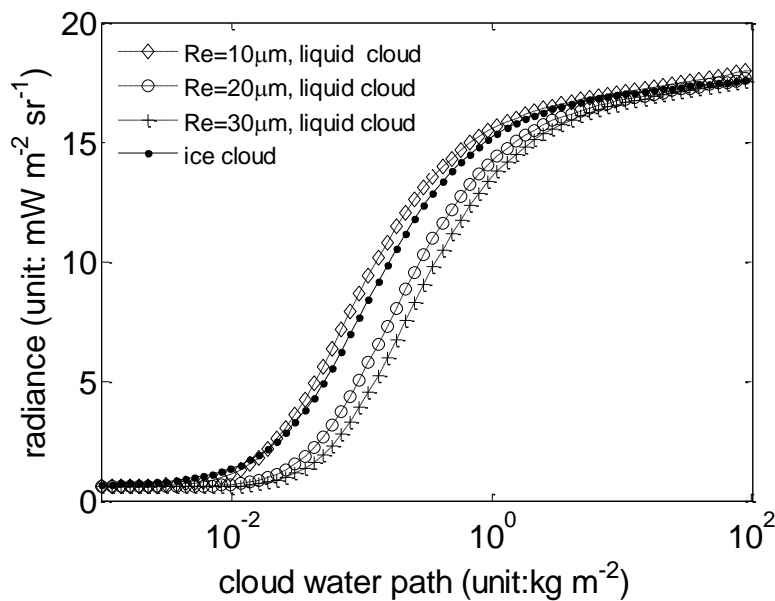
Figure 2. Dependence of AGRI channel 2 radiance on cloud water path and effective radius. The simulation is performed with the "Deff" scheme for liquid water cloud optical properties' calculation and the Baren-2014 scheme for cirrus optical properties' calculation. For this simulation, the solar zenith angle, viewing zenith angle, and relative azimuth angle are set to 25 °, 40 °, and 135 °, respectively.

2.3 DA experiment design and DART configurations

2.3.1 DART filtering algorithm

DART was configured to employ the ensemble adjustment Kalman filter (EAKF, Anderson, 2001) and the rank histogram filter (RHF, Anderson, 2009) algorithms.

EAKF is a serial ensemble DA algorithm and the observations are assimilated as scalars. The model state variable x_m is updated by Equation (1) (Anderson, 2001),

$$x'_m = x_m + \Delta x_{m,n}, \qquad m = 1, \dots, M, n = 1, \dots, N \tag{1}$$

Geoscientific
Model Development
Discussions

where x_m denotes the mth state variable, x'_m the updated value of x_m, and $\Delta x_{m,n}$ the state variable increment for the mth state variable due to the nth observation. $\Delta x_{m,n}$ is calculated by Equation (2),

$$\Delta x_{m,n} = (\sigma_{p,m}/\sigma_p^2)\Delta y_n, \qquad m = 1, \dots, M, n = 1, \dots, N \qquad (2)$$

where the subscript "p" is the abbreviation of "prior", $\sigma_{p,m}$ is the prior sample covariance between the observation and the mth state variable x_m, and σ_p^2 the prior sample variance of the observed variable. Δy_n is the observation increment for the nth observation, which is calculated by the following equation,

$$\Delta y_n = (y_n^p - \bar{y}_p)(\sigma_u/\sigma_p) + \bar{y}_u - y_n^p, \qquad n = 1, \dots, N \qquad (3)$$

where y_n^p denotes the nth prior observation, $\bar{y}_p$ the prior ensemble mean observation, $\bar{y}_u$ the posterior ensemble mean observation, σ_u the updated standard deviation of σ_p. $\bar{y}_u$ and σ_u are calculated by Equations (4) ~ (5).

$$\overline{y_u} = \frac{\sigma_o^2}{\sigma_o^2 + \sigma_p^2}\bar{y}_p + \frac{\sigma_p^2}{\sigma_o^2 + \sigma_p^2}y_o \qquad (4)$$

$$\sigma_u = \frac{\sigma_o \sigma_p}{\sqrt{\sigma_o^2 + \sigma_p^2}} \qquad (5)$$

where y_o and σ_o denote the observation and its corresponding observational error standard deviation.

Anderson (2007; 2009) promoted a spatially varying state-space adaptive covariance inflation to the prior state to increase prior ensemble spread. The same option is adopted in this study and other papers (Lei et al., 2015; Kurzrock et al., 2019). The adaptive inflation uses 1.0, 0.6, and 0.9 as the initial value, fixed standard deviation, and damping settings, respectively. The ensemble size is set to 50. The sampling error due to use of the limited ensemble size was corrected by the method developed by Anderson (2012). The Gaspari-Cohn localization function (Gaspari and Cohn, 1999) with a cutoff of 0.02 radian was used to limit the spread distance of an observation's horizontal influences. Since bulk-layer observations like satellite VIS radiance data do not have a specific single vertical location, no vertical localization was used in this study.

RHF algorithm produces a posterior ensemble based on a continuous approximation of the prior probability density function (PDF) and a piecewise linear representation of the likelihood. The prior PDF is approximated by a rank histogram which has piecewise constant between two ensemble members and follows Gaussian distributions beyond the lower and upper bounds of the ensemble members. Details on how the ensemble members are updated were elaborated in Anderson (2009). The algorithm is declared to be more suitable for non-Gaussian problems.

2.3.2 Pointwise observation DA experiments

To demonstrate the basic ability of the DA scheme, the impact of observations on the WRF model state variables is studied by performing DA experiments with pointwise observations at the four points shown by Figure 1. The analysis time is at 12:40 UTC 18 August 2020, corresponding to the developing stage of the cyclone system. The four points were chosen to represent

different layered cloud structures and cloud phases. The radiance observations for the four points were generated by RTTOV

190 from the nature run at the analysis time.

2.3.3 Cycled DA experiments

Six cycled DA experiments (Exp-1 ~ Exp-6 hereafter) were performed to evaluate the influences of assimilating satellite VIS

radiance observations on cloud simulations. The experiment designs were summarized in table 1. The outlier threshold in table

1 is a pre-defined threshold value for rejecting an observation depending on its distance from the prior ensemble mean. If the

195 distance is more than N (the predefined outlier threshold value) standard deviations from the square root of the sum of the

prior ensemble and observation error variance, the observation is rejected. The DA experiments were designed to explore the

influences of different data properties, filtering algorithms, and cycling variables. Exp-1 and Exp-2 are carried out to reveal

the influences of observation spatial density and updating frequency (small thinning length scale factor and high cycling

interval means more observations are assimilated, and vice versa). Exp-2 and Exp-4 (Exp-3 and Exp-5) are to assess the

200 influences of cycling variables for dense and frequent (sparse and infrequent) observations, Exp-1 and Exp-3 to study the

influences of filtering algorithms, and Exp-2 and Exp-6 to investigate the influences of the outlier threshold values.

Table 1. Parameter settings for six cycled dada assimilation experiments. x_{cloud} denotes the WRF cloud variables including
CLDFRA, QCLOUD, QRAIN, QICE, QSNOW, QGRAUP, QNRAIN, RE_CLOUD, and RE_ICE. x_{atmos} includes atmosphere
thermodynamic variables including U, V, W, PH, T, MU, U10, V10, T2, Q2, PSFC, TH2.

DA experiments	thinning length scale	cycling interval	filtering algorithm	outlier threshold	Cycling variables
Exp-1	60 km	1 hour	EAKF	3	$x_{cloud}+x_{atmos}$
Exp-2	15 km	10 minutes	EAKF	3	$x_{cloud}+x_{atmos}$
Exp-3	60 km	1 hour	RHF	3	$x_{cloud}+x_{atmos}$
Exp-4	15 km	10 minutes	EAKF	3	x_{cloud}
Exp-5	60 km	1 hour	EAKF	3	x_{cloud}
Exp-6	15 km	10 minutes	EAKF	4	$x_{cloud}+x_{atmos}$

205 ### 2.4 Metrics of simulation errors

In this study, WRF state variables simulated by the nature run are deemed theoretical true value. Therefore, the Root Mean

Square Error (RMSE) of a state variable (*x*) is calculated by the following formula,

$$\text{RMSE} = \sqrt{\frac{1}{n_x n_y} \sum_{i,j} \left(x_{i,j}^{\text{sim}} - x_{i,j}^{true} \right)^2} \qquad (6)$$

where $x_{i,j}^{\text{sim}}$ ($x_{i,j}^{true}$) denotes the simulated (true) state variable at the ith (in the zonal direction) and j^{th} (in the meridional direction) model grid. n_x and n_y denote the number of pixels in zonal and meridional directions of the relevant model domains.

Mean absolute error (MAE) is also used to measure the mean distance of the true and the simulated state variables,

$$\text{MAE} = \frac{1}{n_x n_y} \sum_{i,j} abs(x_{i,j}^{\text{sim}} - x_{i,j}^{obs}) \tag{7}$$

The Pearson correlation coefficient is defined as,

$$r = \frac{cov(x^{obs}, x^{sim})}{\sigma_x^{obs} \sigma_x^{sim}} \tag{8}$$

where "cov" denotes the covariance and σ denotes the standard deviation.

The fraction skill score (FSS) is used to assess how well the cloudy or clear areas are represented in simulated fields, which is defined as,

$$\text{FSS} = 1 - \frac{\frac{1}{m_x m_y} \sum_{i,j} \left(p_{i,j}^{obs} - p_{i,j}^{sim} \right)^2}{\frac{1}{m_x m_y} \left[\sum_{i,j} p_{i,j}^{obs} + \sum_{i,j} p_{i,j}^{sim} \right]} \tag{9}$$

where $p_{i,j}^{obs}$ denotes the cloud fraction within a subdomain covering 4×4 model grids. m_x and m_y denote the number of subdomains in the zonal and meridional directions.

Referring to Scheck et al. (2020), the mean profile error (MPE) was calculated by the following formula,

$$\text{MPE} = \frac{1}{p_{\text{sfc}} - p_{top}} \int_{p_{\text{top}}}^{p_{\text{sfc}}} abs[x_{obs}(p) - x_{sim}(p)] dp \tag{10}$$

where p_{sfc} and p_{top} represent pressure at model surface and top, and x denotes an arbitrary model state variable.

Similarly, the mean profile increment (MPI) was used here to evaluate the analysis increment of a vertically distributed state variable.

$$\text{MPI} = \frac{1}{p_{\text{sfc}} - p_{top}} \int_{p_{\text{top}}}^{p_{\text{sfc}}} abs[x_{pos}(p) - x_{pri}(p)] dp \tag{11}$$

where the subscript "pos" and "pri" denote the posterior and prior mean of a certain state variable.

3. Results

3.1 Pointwise data assimilation experiment

In principle, DA procedure adjust the prior ensemble mean radiance (R_{pri}) toward the observed radiance (R_{obs}). However, adjustment of indirect prior ensemble mean model variables, or diagnosed variables such as cloud water path (CWP), according the satellite radiance was rather complicated. The results in Figure 3 show how the state variables were adjusted during a filtering process.
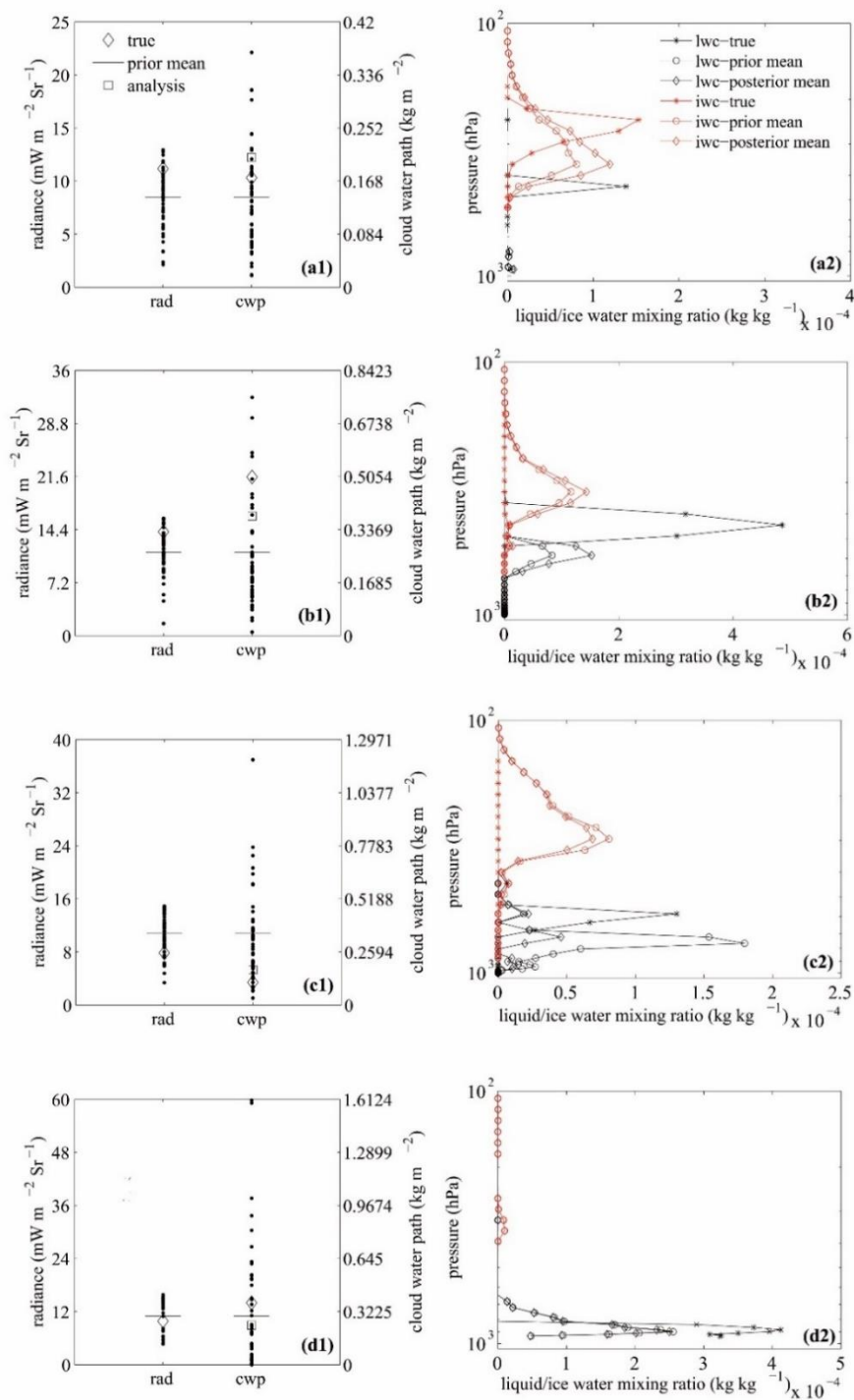
235

Figure 3. Results for the point data assimilation experiments. Column 1: the adjustments of radiance (rad) and cloud water path (cwp). Column 2: the adjustments of liquid water cloud mixing ratio (lwc) and ice cloud mixing ratio content (iwc). From top to bottom, panels 1 ~ 4 denote the results for points 1 ~ 4 shown by Figure 1.

Figure 3(a1,a2) shows the case with $R_{pri} < R_{obs}$. The filtering process updates the prior ensemble mean CWP so that the

240   equivalent prior ensemble mean radiance would be increased. As indicated by Figure 2, radiance at VIS bands is much more

sensitive to CWP than Re. As a result, the prior ensemble mean Re remains unchanged during the filtering procedure (not

shown for simplicity). However, the posterior ensemble mean CWP (w_{pos}) is increased, leading to $w_{pos} > w_{obs} > w_{pri}$, where

w_{obs} and w_{pri} denote the ensemble mean CWP of the true and prior model variables. The results indicate that the CWP is

over-adjusted. This occurred partly due to the nonlinear relationship between CWP and radiance. To be specific, calculating

245   the ensemble mean of Equation (2) and substituting $\overline{y_u}$ with Equation (4) would get the following formula,

$$\overline{\Delta x_m} = \frac{\sigma_{p,m}}{\sigma_o^2 + \sigma_p^2} R_{inc} \tag{12}$$

where Δx_m denotes the ensemble mean of the mth state variable increment, R_{inc} the ensemble mean radiance increment, which

is calculated by Equation (13).

$$R_{inc} = \frac{\sigma_{p,m}}{\sigma_o^2 + \sigma_p^2} (y_o - \bar{y}_p) \tag{13}$$

250   Considering a simplified case with 2 ensemble members, the ensemble mean observation increment is calculated as the

following formula,

$$R_{inc} = \frac{\sigma_p^2}{\sigma_o^2 + \sigma_p^2} [F(w_{obs}) - \frac{F(w_1) + F(w_2)}{2}] \tag{14}$$

where F denotes the forward observation operator. w_1 and w_2 represent CWP of the two ensemble members.

However, considering the relationship between CWP and the VIS radiance, the theoretical true observation increment

255   should be,

$$R_{inc}^t = \frac{\sigma_p^2}{\sigma_o^2 + \sigma_p^2} [F(w_o) - F(\bar{x})], \bar{x} = \frac{w_1 + w_2}{2} \tag{15}$$

As indicated by Figure 4, R_{inc} is larger than R_{inc}^t. Namely, the ensemble mean observation increment was overestimated

by Equation (14), leading to an over-estimated posterior ensemble mean CWP as depicted by Figure 3(a).

For $R_{obs} < R_{pri}$, the prior ensemble mean Re was almost unchanged and CWP was decreased (Figure 3(d1,d2)), which

260   is in favor of a negative ensemble mean of the observation increment. The result $w_{pos} < w_{pri} < w_{obs}$ could be also partly

explained by the nonlinearity of the observation operators.

Figure 3(b1,b2) and 3(c1,c2) represent two "idealized" adjustments. Namely, w_{pos} is within the range bounded by w_{pri}

and w_{obs} given that Re is almost unchanged during the filtering process. In these two cases, assimilating radiance data

improves the vertically accumulated cloud water/ice mixing ratio (equivalent to CWP), but it could not adjust the vertical

265   positions of the clouds. In addition, the direct assimilation could not improve cloud phase simulations. For point 2, the truth

state shows a thin liquid water cloud spanning from 500 ~ 450 hPa but both the prior and posterior show a two-layered structure,

including an upper ice cloud layer spanning from 500 ~ 200 hPa and a lower liquid water cloud layer spanning from 700 ~ 500 hPa. In other words, there is a one-layered liquid water cloud in the true state but a two-layered cloud structure in the prior and posterior fields. Such phenomena were also reported by previous studies where they ascribe the failure to the fact that satellite
270   VIS radiance is insensitive to the particular cloud vertical structure (Scheck et al., 2020).
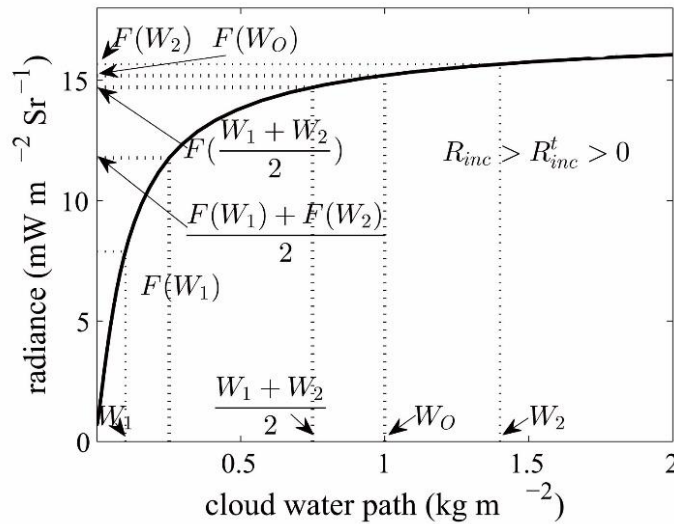
Figure 4. Illustration of the effects of nonlinearity of the observation operator on calculation of radiance increments with 2 ensemble members. F denotes the observation operator, W_1 and W_2 denote cloud water path (CWP) for the 1st and 2nd ensemble member,
275   **W_O denotes the observed CWP. R_{inc} denotes the calculated ensemble mean radiance increment, and R_{inc}^t denotes the true radiance increment which respect the laws between the CWP and the radiance.**

The EAKF algorithm assumes that the prior ensemble estimates of a scalar observation y_p (radiance in this study) confirms to a Gaussian distribution $N(\overline{y_p}, \sigma_p^2)$. To see how well the approximation was respected, the Probability Density
280   Functions (PDFs) of y_p for the four points are presented in Figure 5. As indicated, the non-Gaussian characteristics are apparent, especially for the Point 4. Therefore, a DA experiment using the the RHF filtering algorithm was added in comparison with EAKF.
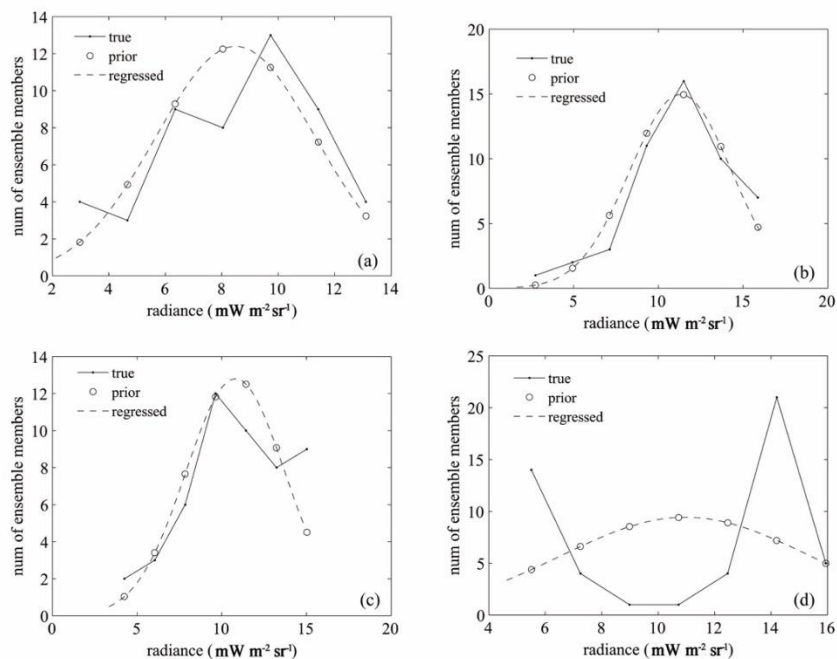
Figure 5. The probability density functions of the radiance for the prior ensemble members for the four points shown by Figure 1.
285 **(a) ~ (d) correspond to Points 1 ~ 4.**

3.2 Cycled DA experiments

3.2.1 Influences on CWP

The time evolution of CWP for the nature run, control run, Exp-2, and Exp-4 are presented by Figure 6. Quantitative
290 comparison results for Exp-1 ~ Exp-5 are summarized in Figure 7.
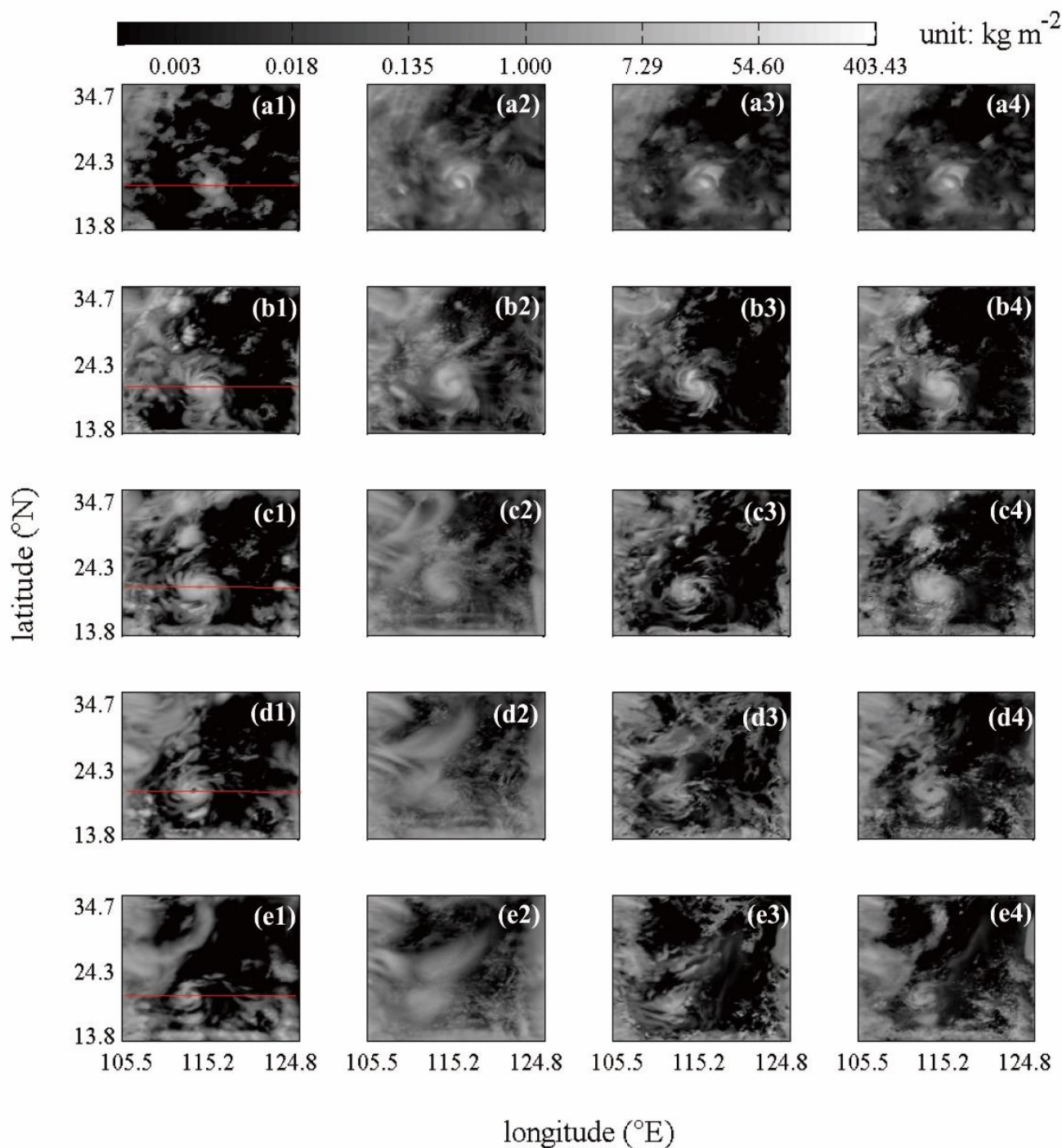
Figure 6. Time evolution of cloud water path (CWP) for the nature run (column 1), the control run (column 2), Exp-2 (column 3), and Exp-4 (column 4). From top to bottom, the row panels correspond to 12:40 UTC 18 August 2020, 15:40 UTC 18 August 2020, 18:40 UTC 18 August 2020, 21:40 UTC 18 August 2020, and 00:40 UTC 19 August 2020, respectively. The red lines in the first column are for cross-section analyses.
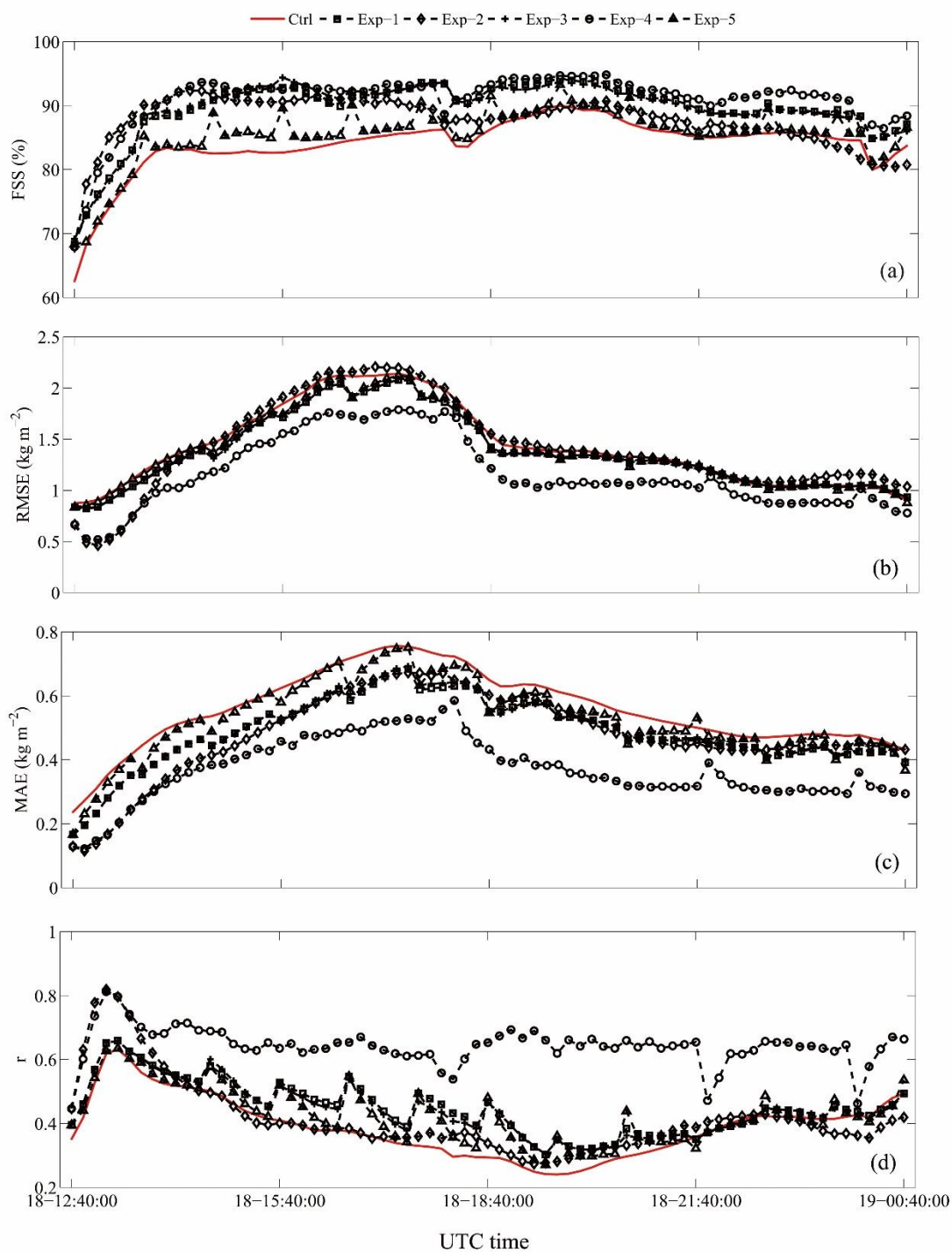
295

Figure 7. Quantitative metrics for the control run and Exp-1 ~ Exp-5. (a) ~ (d) denote the fraction skill score (FSS), the root mean square error (RMSE), and the mean absolute error (MAE) of the posterior ensemble mean cloud water path (CWP), and the Pearson correlation coefficient (r) between the posterior ensemble mean cloud water path (CWP) and the true CWP.

The FSS results indicate that assimilating VIS radiance improves cloud coverage simulations in most cases. In comparison with the control run, assimilating VIS radiance data could clearly suppress the wrong clouds in the regions where it is cloudy for the control run but are clear for the nature run. However, for regions which are clear for the prior ensemble mean but cloudy for the nature run, assimilating the VIS radiance data could not generate cloud hydrometers (Figure 6). This is because the

305   increments for each state variable are calculated by regressing the observation increments on the state variables through the covariance between the observations and the state variable. The covariance between the observations and the state variable is zero in cloudless regions of the prior and thus, the observation increments cannot be mapped to the state variables.

In terms of the whole cyling period, Exp-1 and Exp-3 almost coincide and achieved consistently positive results. Exp-1 and Exp-3 differ in filtering algorithms. Therefore, it seems that RHF does not outperform EAKF in cloud coverage simulations.

310   A potential explanation is that despite RHF deals with non-Gaussian problems better than EAKF, its advantages may be subject to the limited number of ensemble members (50 in this study). In addition, Exp-1 achieved better results than Exp-5. The differences of the two experiments lie in the cycling variables. Given the fact that using the multi-variable atmosphere state analysis increments into the ensemble forward integration cycles degrades cloud simulations, DA of VIS radiance data may cause negative influences on some atmosphere thermodynamic state variables. The negative impacts on atmosphere

315   thermodynamic state variables were also revealed by comparing Exp-2 and Exp-4, where exp-4 corresponds to the best results in general.

The RMSEs, MAEs, and Pearson correlation coefficients (r) of the experiments present some different characteristics to FSSs. It is apparent that best results were achieved for Exp-4, which assimilates VIS radiance with high-frequency (10 minute) update cycles. Exp-2 differs from Exp-4 in that Exp-2 includes both cloud and atmosphere thermodynamic variable analysis

320   increments in ensemble forward integration, but Exp-4 only includes the cloud analysis increments. CWP simulations for Exp-4 is evidently better than Exp-2, indicating that assimilating VIS radiance data has negative influences on some atmosphere thermodynamic state variables for dense observations with high updating frequency. Because satellite VIS radiance data have no apparent dependence on atmosphere thermodynamic state variables, errors could be induced to atmosphere thermodynamic state variables during the filtering processes through fake correlation between VIS radiance and these variables. On the other

325   hand, Exp-5 and Exp-1 are similar to the Exp-4 vs Exp-2 pair but with lower update frequency (60 minutes) and thinner observations. The forecasting skill of CWP is slightly better for Exp-1 than Exp-5, indicating slightly positive influences on some atmosphere state variables in this case, which agrees with Scheck et al. (2020). The overall results for FSS, RMSE, MAE, and r show that assimilating VIS radiance data generally cause negative influences on atmosphere thermodynamic state variables for dense observations with high updating frequency, but for sparse observations with low updating frequency, such

330   impact is insignificant. The RMSE, MAE, and r results for Exp-1 and Exp-3 are close, which is similar to the results for FSS. Therefore, RHF algorithm is comparable to EAKF algorithm for assimilating the VIS radiance data in cloudy regions.

To compare the model clouds in the horizontal and vertical directions, we analyze Figure 8, which gives the *x-pressure* cross sections of mixing ratio of the total liquid/ice hydrometers along the red lines in Figure 6.

Geoscientific
Model Development
Discussions
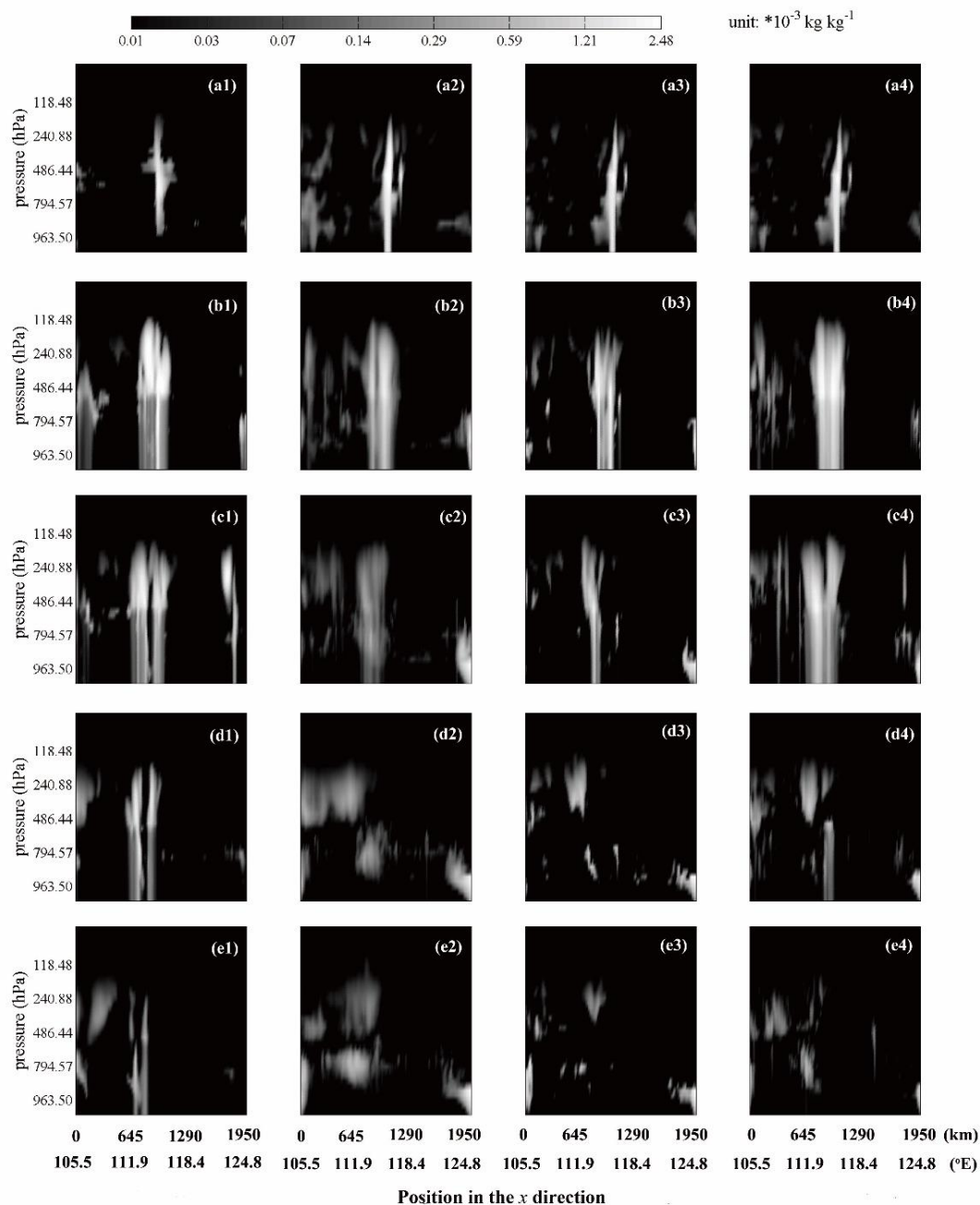
Figure 8. The x-press cross section of cloud water/ice mixing ratio for the red line shown by Figure 6 (c1). From left to right, the column panels correspond to the nature run, control run, Exp-2, and Exp-4. From top to bottom, the row panels correspond to 12:40 UTC 18 August 2020, 15:40 UTC 18 August 2020, 18:40 UTC 18 August 2020, 21:40 UTC 18 August 2020, and 00:40 UTC 19 August 2020, respectively. These times corresponds to those in Figure 6.

At the initial cycling step, a convective initiation was generated by the nature run. At this stage, no precipitation was found at the sea surface (Figure 8(a1)). However, precipitation was found in the control run (Figure 8(a2)). After the EAKF

filtering, the updated cloud fields suggested precipitation at the sea surface (Figure 8(a3) ~ Figure 8(a4)). Nevertheless, some fake clouds between 100 and 400 km in the x direction (Figure 8(a2)) were eliminated in the posterior ensemble mean cloud fields. The results imply that although assimilating satellite VIS radiance data could not adjust cloud and precipitation in the vertical directions, but it helps to improve the horizontal cloud and precipitation distribution.

345   At 15:40 UTC 18 August 2020, the control run is pretty close to the nature run, except that some fake clouds were generated in the location between 200 ~ 400 km (Figure 8(b2)). These clouds were clearly suppressed in Exp-2 and Exp-4 (Figure 8(b3) and Figure 8(b4)). Comparison within Exp-2, Exp-4 and the nature run indicate that the cyclone cloud area is underestimated by Exp-2. This is because Exp-2's atmosphere thermodynamic state variables are updated in negative ways as aforementioned, which may cause counteracting effects to cloud development. At 18:40 UTC 18 August 2020, a clear "eye"

350   structure" was presented at ~ 900 km in the *x* direction in the nature run (Figure 8(c1)). This structure was not simulated by the control run (Figure 8(c2), Figure 6(c2)) and Exp-2 (Figure 8(c3), Figure 6(c3)) and the other DA experiments except for Exp-4. At this stage, the cyclone cloud system was further shrunk in Exp-2. In contrast, Exp-4 captures well the "eye" structure (Figure 8(c4), Figure 6 (c4)) and the cyclone cloud areas.

        At 21:40 UTC 18 August 2020, the cyclone cloud area was shrunk and entered the dissipating stage. The "eye" structure

355   is still apparent for the nature run (Figure 8(d1), Figure 6(d1)). Exp-4 continues to properly simulate the "eye structure" and cloud coverage of the cyclone (Figure 8(d4), Figure 6(d4)), although the precipitation in the left side of the "eye" was not generated, and the one-layered cloud and precipitation structure in the right side of the "eye" was mis-simulated as a two-layered structure. These results further confirm that assimilating VIS radiance improves the cloud amount in the horizontal directions but not in the vertical. In contrast, the control run and Exp-2 only produce some weak non-precipitating cloud,

360   seriously underestimating the cyclone cloud system.

        At 00:40 UTC 19 August 2020, the cyclone precipitation persists in the nature run (Figure 8(e1)). However, the precipitation was not simulated in any of the DA experiments (Figure 8(e3) and Figure 8(e4)). In comparison to the control run which generates some false clouds around 650 km (Figure 8(e2)), assimilating the VIS radiance data gain a cloud coverage much more close to the nature run (Figure 8 (e4) and Figure 6(e4)).

365   **3.2.2 Influences on Re**

The time evolution of MPIs and MPEs of Re for Exp-2 are presented by Figure 9. MPIs of Re are within 1 μm at most analysis times (Figure 9(a)). In addition, MPEs of Re are within 15 μm (Figure 9(b)). In fact, Re is underestimated at most of the analysis times. At 18:40 UTC, 18 August 2020, Re is underestimated near the cyclone's center (Figure 10(a)). In order to increase the radiance comparable with the observations, either positive CWP increments or negative Re increments should be

370   generated. In this case, Re is underestimated and Re increments are approximately zero (Figure 10(b)). Combing the Figure 9(a) and Figure 10(b), we may draw a conclusion that DA of VIS radiance data has trivial influences on Re. Because satellite VIS radiance is positively (negatively) related to CWP (Re) (Figure 2), the CWP increment is not as large as that expected for the Re equal to the observed value. This could partly explain the phenomenon why CWP near the cyclone center is

underestimated (Figure 8(c3), Figure 6(c3)). Similar results were found for the other DA experiments. For brevity, they are
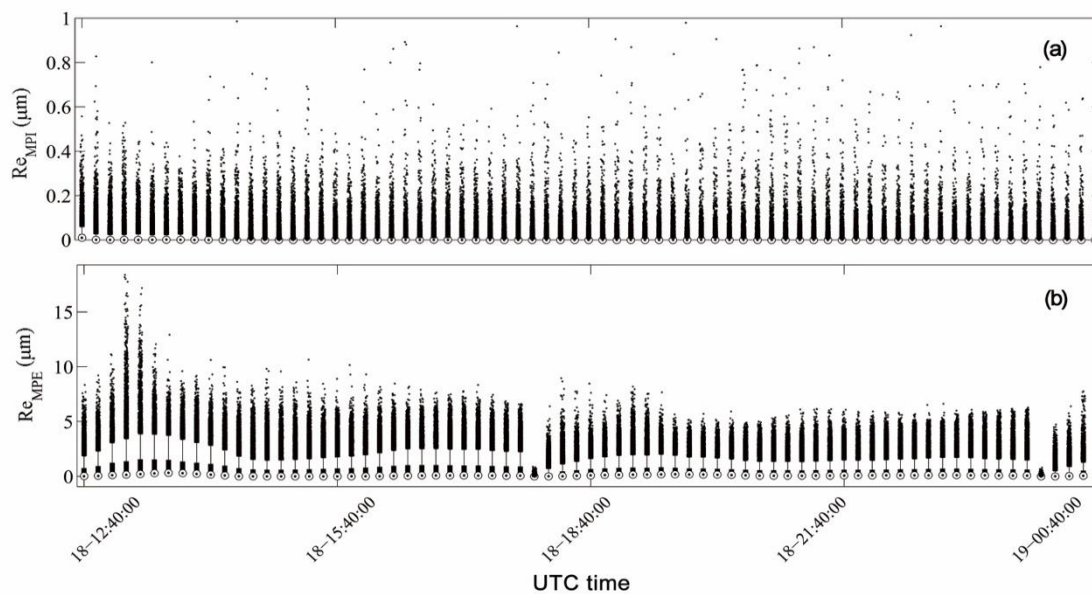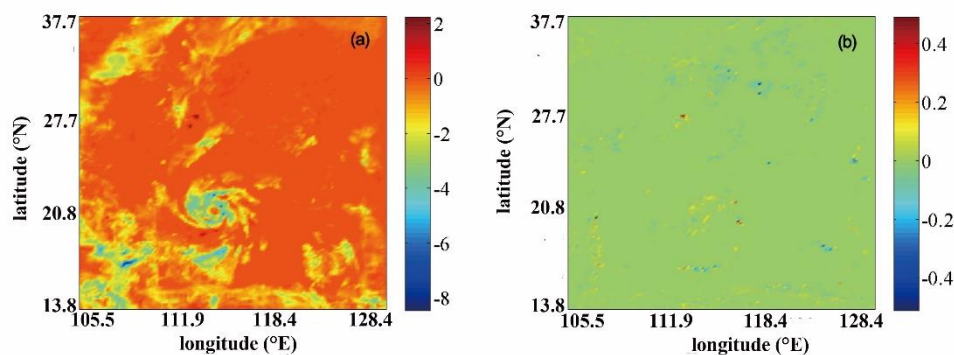
375   not presented here.

Figure 9. Time evolution of (a) mean profile increment (MPI), defined by Equation (11), and (b) mean profile error (MPE), defined by Equation (10), of Re for Exp-02.

380

Figure 10. (a) the mean profile error (without absolute operation) and (b) the mean profile increment (without absolute operation) of Re for Exp-2 at the analysis time 18:00 UTC, 18 August 2020.
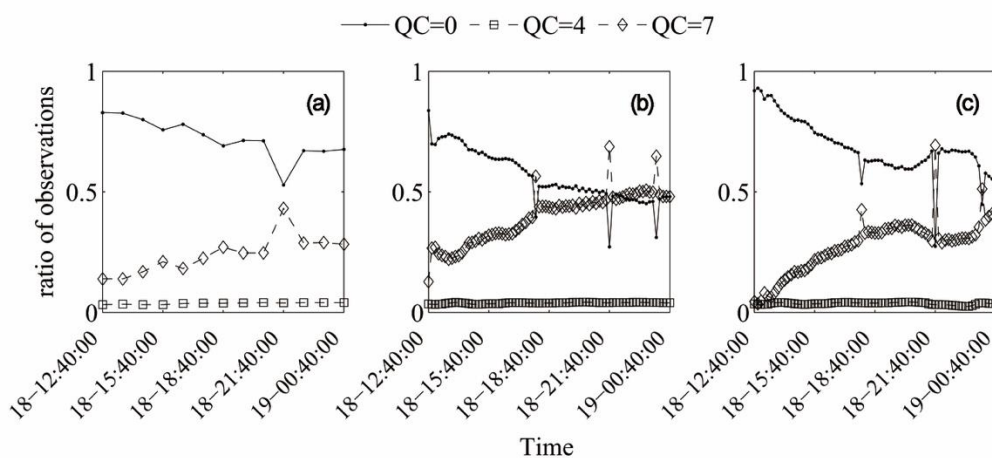
4. Discussions on observation rejection

It is noteworthy that not all observations are effectively assimilated by the WRF/DART-RTTOV system during the filtering

385   process. Two types of the observations are rejected, including (1) the observations that are too far from the prior ensemble

mean (e.g., QC = 7) because assimilating these data may cause the collapse of WRF model and (2) those resulting in state variables that do not satisfy some basic physical laws (QC = 4), e.g., non-monotonic pressure.

Figure 11 shows the ratios of observations that are assimilated (or rejected) for different reasons. In the present case, non-monotonic pressure was mainly located in the Qinghai-Tibet Plateau, Tianshan Mountain, and Central Taiwan ranges (not

390   shown for simplicity), where complex terrain exists. Observations corresponding to the non-monotonic pressure account for 4% of all. The non-monotonic pressure was generated during interpolation of the perturbed model states.

The number of "far observations" was increased with time evolution, implying that the differences between observation and the prior ensemble mean are increased over time. For DA experiments which include atmospheric thermodynamic state variables as cycling variables, such a phenomenon could be ascribed to the forecasting errors of atmospheric thermodynamic

395   state variables due to fake correlation between VIS radiance and these variables. In general, about 80% observations were assimilated by DART system in the initial assimilation cycles for Exp-1 ~ Exp-5 (The results for Exp-1 and Exp-2 are shown by Figure 11(a) and 11(b), respectively). As the DA cycles move on, the percentage decreased to about 50%.

Figure 11. The ratio of observations assimilated (QC=0) or rejected (QC=4 or QC=7) by DART for (a) Exp-1, (b) Exp-2, and (c)
400   **Exp-6.**

DART uses a predefined threshold value (*outlier_threshold*) to determine whether an observation should be rejected or assimilated. Larger *outlier_threshold* allows more observations accepted by DART. The threshold value is set to 3.0 in Exp-1 ~ Exp-5, corresponding to a usage of a small number of observations at the mid and late cycling stages. To increase the usage

405   efficiency, *outlier_threshold* was set to 4.0 for Exp-6. As indicated by Figure 11(c), large *outlier_threshold* do increase the usage efficiency of observations. The corresponding influences on cloud simulations (Figure 12) indicate that assimilating more observations do not result in improvements to cloud simulations. A potential explanation is that the positive effects on cloud state variables with more observation were counteracted by the negative effects on atmosphere thermodynamic state

variables. After several cycling steps, errors of atmosphere thermodynamic state variables are accumulated, and the errors of

410 cloud simulations are drastically enlarged. For example, the maximum RMSE of CWP could reach as large as 4.3 kgm^{-2}.
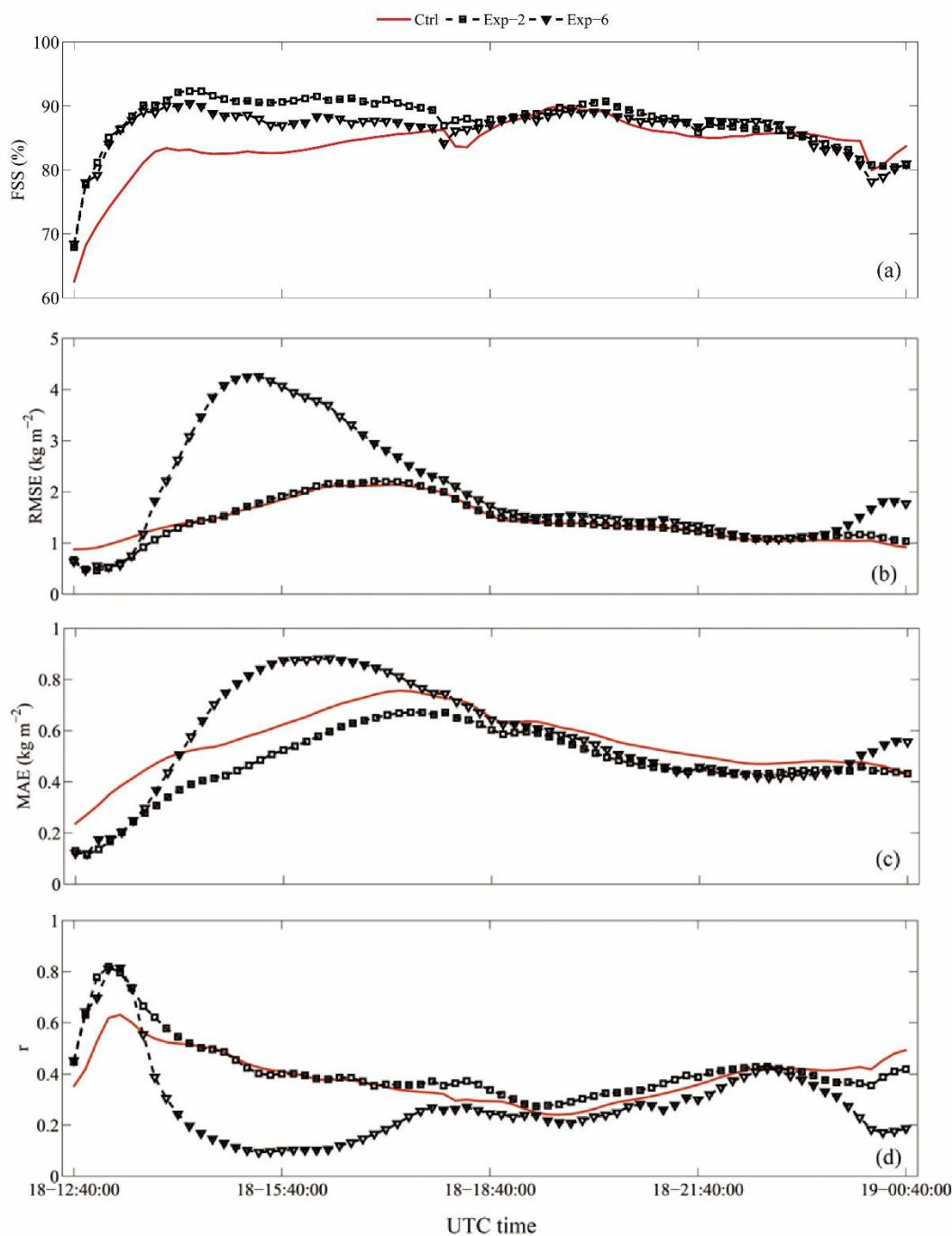

Figure 12. Verification metrics for Exp-2 and Exp-6 for posterior ensemble mean CWP. (a) ~ (d) denote the fraction skill score (FSS), the root mean square error (RMSE), the mean absolute error (MAE), and the Pearson correlation coefficient (r).

21

Therefore, *outlier_threshold* should be set with caution to properly trade off the benefits to cloud assimilation and its
415 negative influences on the atmospheric thermodynamic states. On one hand, DART should be set to assimilate as much
observations as possible to improve cloud forecasting skills. On the other hand, measures should be taken to avoid the
detrimental effects due to forecasting errors of atmosphere state variables caused by the DA processes. There are two possible
solutions to this problem. One method is to discard atmosphere state variables in the cycling variables for dense observations
with high updating frequency, as is performed by Exp-4. Another method is to collaboratively assimilate other complementary
420 observations, such as the atmospheric Motional Vector (AMV) derived from continuous satellite images, to suppress the
negative influence of the VIS radiance DA on the atmospheric thermodynamic states.

5. Conclusion

In this study, OSSEs were performed to investigate the ability of the WRF/DART system along with the RTTOV observation
operator for assimilating FY-4/AGRI VIS (channel 2) radiance data. Six DA experiments were designed to study the impacts
425 of different observation densities and updating frequencies, filter algorithms, *outlier_threshold* values, and cycling variables.
The modeling experiments cover the strengthening and weakening processes of a cyclone case. Influences of assimilating VIS
radiance data on cloud simulations were evaluated. Main results and findings are summarized below.

(1). The DART filtering processes mainly influence CWP, with little impact on Re. The adjustments of CWP has
significant positive influences on cloud simulations in the horizontal directions. Because VIS radiance is insensitive to the
430 cloud vertical structures, there is no direct constraint to adjust the cloud water/ice content to the proper height. In some
scenarios, the filtering process may cause negative CWP adjustments, namely, the posterior ensemble mean CWP is out of the
range bounded by the prior ensemble mean and the observations. These negative adjustments are partially caused by the
nonlinear relationship between radiance and CWP. This problem could be potentially solved by the particle filter-based DA
approaches (Shen and Tang, 2014; Pinheiro et al., 2019).

435 (2). On the domain average, assimilating VIS radiance improves cloud simulations at most of the analysis times. The best
cloud forecasting skills were found for dense observations with high updating frequency, and with cloud state variables (x_{cloud})
as the cycling variables. For the data assimilation of dense and high-frequency observations, the atmosphere thermodynamic
state variables (x_{atmos}) should not be taken as the cycling update variables because the adjustments of x_{atmos} by VIS radiance
DA introduce negative influences on cloud simulations.

440 (3). Many observations were discarded by the WRF/DART-RTTOV system, with a loss of up to 50% of available VIS
radiance observations. Most of the observations rejected are too far from the prior ensemble mean (according to the predefined
threshold value *outlier_threshold*). Some other observations, mainly over complex terrain regions, are rejected because non-
monotonic pressure detected.

In addition, there are two major shortcomings with the current VIS radiance DA approach: one is its inability to improve
445 cloud vertical distribution and the other is its inability to influence atmosphere thermodynamic state variables positively. In

this study, the observation operator is assumed to be quite accurate with an observation error of 1 mW m^{-2} sr^{-1}. This assumption is proper for the coarse grid spacing (15 km in this study) as 3D radiative effects are trivial at this scale (Várnai and Marshak, 2001). However, most of the operational observation operators would introduce non-negligible errors for small grid spacing such as convective scale resolutions due to 3D radiative effects (Zhou et al., 2021). In addition, increasing model

450 grid spacing would introduce other problems such as the enhanced nonlinearity effects and physical consistency between nested domains (Kurzrock et al., 2019). Extending the present research to solve these problems with WRF-DART/RTTOV should be taken.

Code and data availability

Version 4.1.1 of WRF-ARW source code is publicly available at http://www2.mmm.ucar.edu/wrf/users/. The Manhattan release

455 of DART source code (version 9.8.0), including the RTTOV observation operator (version 12.3), is publicly available at https://dart.ucar.edu/.   Version   12.3   of   RTTOV   source   code   is   publicly   available   at   https://nwp-saf.eumetsat.int/site/software/rttov/. The NCEP FNL (Final) Operational Global Analysis data are downloaded from https://rda.ucar.edu/datasets/ds083.2/.   The   ERA5   hourly   data   are   available   at https://cds.climate.copernicus.eu/api/v2/resources. The source codes of WRF-ARW, WPS, RTTOV, and DART models (tool),

460 as well as the input and (processed) output data, the visualization scripts, along with a readme file corresponding to each file are available at https://zenodo.org/record/6417682#.YlEKbX5BzIU.

Author contribution

Yongbo Zhou: Conceptualization, Methodology, Writing original draft, Visualization, Funding acquisition. Yubao Liu: Conceptualization, review and editing. Zhaoyang Huo, review and editing. Yang Li, review and editing.

465 **Competing interests**

The authors declare that they have no conflict of interest.

Acknowledgement

References

Anderson, J. L.: An Ensemble Adjustment Kalman Filter for Data Assimilation, Mon. Weather Rev., 129, 2884-2903,
475   doi:10.1175/1520-0493(2001)129<2884:AEAKFF>2.0.CO;2, 2001.

Anderson, J. L.: An adaptive covariance inflation error correction algorithm for ensemble filters, Tellus A, 59, 210-224,
        doi:10.1111/j.1600-0870.2006.00216.x, 2007.

Anderson, J. L.: Spatially and temporally varying adaptive covariance inflation for ensemble filters, Tellus A, 61, 72–83,
        doi:10.1111/j.1600-0870.2008.00361.x, 2009.

480 Anderson, J. L.: Localization and Sampling Error Correction in Ensemble Kalman Filter Data Assimilation, Mon. Wea. Rev.,
        140(7), 2359-2371, doi:10.1175/MWR-D-11-00013.1.

Anderson, J., Hoar, T., Raeder, K., Liu, H., Collins, N., Torn, R., and Avellano, A.: The Data Assimilation Research Testbed:
        A Community Facility, B. Am. Meteorol. Soc., 90(9), 1283-1296, doi:10.1175/2009BAMS2618.1, 2009.

Baren, A. J., Cotton, R., Furtado, K., Havemann, S., Labonnote, L.-C., Marenco, F., Smith, A., and Thelen. J.-C.: A self-
485   consistent scatteringmodel for cirrus. II: The high and low frequencies, Q. J. R. Meteorol. Soc., 140: 1039-1057,
        doi:10.1002/qj.2193, 2014.

Bauer, P., Ohring, G., Kummerow, C., and Auligne, T.: Assimilating satellite observations of clouds and precipitation into
        NWP models, B. Am. Meteorol. Soc., 92, ES25-ES28, doi:10.1175/2011BAMS3182.1, 2011.

Betts A. K., and Miller M. J.: The Betts-Miller Scheme. In: Emanuel K.A., Raymond D.J. (eds) The Representation of Cumulus
490   Convection in Numerical Models, Meteor. Monogr., No. 24, Amer. Meteor. Soc., Boston, MA., 107-121,
        doi:10.1007/978-1-935704-13-3_9, 1993.

Coste, P., Pasternak, F., Faure, F., Jacquet, B., Bianchi, S., Aminou, D. M. A., Luhmann, H. J., Hanson, C., Pili, P., and Fowler,
        G.: SEVIRI, the imaging radiometer on Meteosat second generation: in-orbit results and first assessment, Proceedings of
        the SPIE, 10568, 105680L, doi:10.1117/12.2308023, 2017.

495 Ek, M. B., Mitchell, K. E., Lin, Y., Rogers, E., Grunmann, P., Koren, V., Gayno, G., and Tarpley, J. D.: Implementation of
        Noah land surface model advances in the National Centers for Environmental Prediction operational mesoscale Eta model,
        J. Geophys. Res., 108(D22), 8851, doi:10.1029/2002JD003296, 2003.

Gaspari, G. and Cohn, S. E.: Construction of correlation functions in two and three dimensions, Q. J. R. Meteorol. Soc.,
        125(554), 723-757, doi:10.1002/qj.49712555417, 1999.

500 Geer, A.J., Migliorini, S., and Matricardi, M.: All-sky assimilation of infrared radiances sensitive to mid- and upper-
        tropospheric moisture and cloud, Atmos. Meas. Tech., 12, 4903-4929, doi:10.5194/amt-12-4903-2019, 2019.

Hasselmann, K., Barnett, T. P., Bouws, E., Carlson, H., Cartwright, D. E., Enke, K., Ewing, J. A., Gienapp, H., Hasselmann,
        D. E., Kruseman, P., Meerburg, A., Müller, P., Olbers, D. J., Richter, K., Sell, W., Walden, H.: Measurements of wind-
        wave growth and swell during the Joint North Sea Wave Project (JONSWAP), Deutches Hydrographisches Institut, 12,
505   95 pp., http://resolver.tudelft.nl/uuid:f204e188-13b9-49d8-a6dc-4fb7c20562fc, 1973

Hong, S.-Y. and Pan, H.-L.: Nonlocal Boundary Layer Vertical Diffusion in a Medium-Range Forecast Model, Mon. Weather Rev., 124, 2322-2339, doi:10.1175/1520-0493(1996)124<2322:NBLVDI>2.0.CO;2, 1996.

Iacono, M. J., Delamere, J. S., Mlawer, E. J., Shephard, M. W., Clough, S. A., and Collins, W. D.: Radiative forcing by long-lived greenhouse gases: Calculations with the AER radiative transfer models, J. Geophys. Res., 113, D13103, doi:10.1029/2008JD009944, 2008.

Janjić, Z. I.: The step-mountain eta coordinate model: Further development of the convection, viscous sublayer, and turbulence closure schemes. Mon. Wea. Rev., 122, 927-945, doi:10.1175/1520-0493(1994)122<0927:TSMECM>2.0.CO;2, 1994.

Janjić, Z. I.: The surface layer in the NCEP Eta model. 11th Conf. on Numerical Weather Prediction, Norfolk, VA, 19–23 August, Amer. Meteor. Soc., Boston, MA, 354–355, 1996.

Keat, W. J., Stein, T. H. M., Phaduli, E., Landman, S., Becker, E., Bopape, M.-J. M., Hanley, K. E., Lean, H. W., Webster, S.: Convective initiation and stormlife cycles in convection-permitting simulations of the Met Office Unified Model over South Africa, Q. J. R. Meteorol. Soc., 145, 1323-1336, doi:10.1002/qj.3487, 2019.

Kong, R., Xue, M., and Liu, C. S.: Development of a Hybrid En3DVar Data Assimilation System and Comparisons with 3DVar and EnKF for Radar Data Assimilation with Observing System Simulation Experiments, Mon. Wea. Rev., 146(1), 175-198, doi:10.1175/MWR-D-17-0164.1, 2018.

Kostka, P. M., Weissmann, M., Buras, R., Mayer, B., and Stiller, O.: Observation operator for visible and near-infrared satellite reflectances, J. Atmos. Ocean. Tech., 31(6), 1216-1233, doi:10.1175/JTECH-D-13-00116.1, 2014

Kurzrock, F., Nguyen, H., Sauer, J., Ming, F. C., Cros, S., Smith Jr. W. L., Minnis, P., Palikonda, R., Jones, T. A., Lallemand, C., Linguet, L., and Lajoie, G.: Evaluation of WRF-DART (ARW v3.9.1.1 and DART Manhattan release) multiphase cloud water path assimilation for short-term solar irradiance forecasting in a tropical environment, Geosci. Model Dev., 12, 3939-3954, doi:10.5194/gmd-12-3939-2019, 2019.

Lei, L., Anderson, J. L., and Romine, G. S.: Empirical Localization Functions for Ensemble Kalman Filter Data Assimilation in Regions with and without Precipitation, Mon. Wea. Rev., 143(9), 3664-3679, doi:10.1175/MWR-D-14-00415.1, 2015.

Lei, L., Wang, Z., and Tan, Z.-M., Integrated Hybrid Data Assimilation for an Ensemble Kalman Filter, Mon. Wea. Rev., 149(12), 4091-4105, doi:10.1175/MWR-D-21-0002.1, 2021.

Lim, K.-S. S. and Hong, S.-Y.: Development of an effective double-moment cloud microphysics scheme with prognostic cloud condensation nuclei (CCN) for weather and climate models, 138(5): 1587-1612, doi:10.1175/2009MWR2968.1, 2010.

Ma, Z., Maddy, E. S., Zhang, B., Zhu, T., Boukabara, S. A.: Impact Assessment of Himawari-8 AHI Data Assimilation in NCEP GDAS/GFS with GSI, J. Atmos. Ocean. Tech., 34(4), 797-815, doi:10.1175/JTECH-D-16-0136.1, 2017.

Mansell, E. R., Ziegler, C. L., and Bruning, E. C.: Simulated Electrification of a Small Thunderstorm with Two-Moment Bulk Microphysics. J. Atmos. Sci., 67(1), 171-194. doi:10.1175/2009JAS2965.1, 2010.

Matricardi, M.: The generation of RTTOV regression coefficients for IASI and AIRS using a new profile training set and a new line-by-line database, ECMWF, Technical Memorandum, 564, 47 pp., https://doi.org/10.21957/59u3oc9es, 2008.

Mayer, B. and Kylling, A.: Technical note: The libRadtran software package for radiative transfer calculations—description and examples of use, Atmos. Chem. Phys., 5, 1855–1877,doi:10.5194/acp-5-1855-2005, 2005

Migliorini, S. and Candy, B.: All-sky satellite data assimilation of microwave temperature sounding channels at the Met Office, Q. J. R. Meteorol. Soc., 145(719), 867-883, doi:10.1002/qj.3470, 2019.

Nakajima T. and King, M. D.: Determination of the optical thickness and effective particle radius of clouds from reflected solar radiation measurements. Part I: Theory. J. Atmos. Sci., 47(15): 1878-1893, doi:10.1175/1520-0469(1990)047<1878:DOTOTA>2.0.CO;2, 1990.

Pinheiro, F. R., van Leeuwen, P. J., and Geppert, G.: Efficient nonlinear data assimilation using synchronization in a particle filter, Q. J. R. Meteorol. Soc., 145:2510-2523, doi:10.1002/qj.3576.

Polkinghorne, R. and Vukicevic, T.: Data assimilation of cloud-affected radiances in a cloud-resolving model, Mon. Wea. Rev., 139(3), 755-773. doi:10.1175/2010MWR3360.1, 2011.

Saunders, R., Hocking, J., Turner, E., Rayer, P., Rundle, D., Brunel, P., Vidot, J., Roquet, P., Matricardi, M., Geer, A., Bormann, N., and Lupu, C.: An update on the RTTOV fast radiative transfer model (currently at version 12). Geosci. Model Dev., 11(7), 2717-2737, doi:10.5194/gmd-11-2717-2018, 2018.

Scheck, L.: A neural network based forward operator for visible satellite images and its adjoint, J. Quant. Spectrosc. Radiat. Transf., 274, 107841, doi:10.1016/j.jqsrt.2021.107841, 2021.

Scheck, L., Fràebeau, P., Buras-Schnell, R., and Mayer, B.: A fast radiative transfer method for the simulation of visible satellite imagery, J. Quant. Spectrosc. Radiat. Transf., 175, 54-67. doi:10.1016/j.jqsrt.2016.02.008, 2016a.

Scheck, L., Hocking, J., and Saunders, R.: A comparison of MFASIS and RTTOV-DOM. Report of Visiting Scientist mission NWP_VS16_01 (Document ID, NWPSAF-MO-VS-054), EUMETSAT. Retrieved from https://nwpsaf.eu/vs_reports/nwpsaf-mo-vs-054.pdf, 2016b.

Scheck, L., Weissmann, M., and Bernhard, M.: Efficient Methods to Account for Cloud-Top Inclination and Cloud Overlap in Synthetic Visible Satellite Images, J. Atmos. Ocean. Tech., 35, 665-685, doi:10.1175/JTECH-D-17-0057.1, 2018.

Scheck, L., Weissmann, M., and Bach, L.: Assimilating visible satellite images for convective-scale numerical weather prediction: A case-study, Q. J. R. Meteorol. Soc., 146(732), 3165-3186, doi:10.1002/qj.3840, 2020.

Schmit, T. J., Lindstrom, S. S., Gerth, J. J., and Gunshor, M. M.: Applications of the 16 spectral bands on the Advanced Baseline Imager (ABI), J. Operational Meteor., 6 (4), 33-46, doi:10.15191/nwajom.2018.0604, 2018.

Schröttle, J., Weissmann, M., Scheck, L., and Hutt, A.: Assimilating Visible and Infrared Radiances in Idealized Simulations of Deep Convection, Mon. Wea. Rev., 148(11), 4357-4375, doi:10.1175/MWR-D-20-0002.1, 2020.

Shen, Z. and Tang, Y.: A modified ensemble Kalman particle filter for non-Gaussian systems with nonlinear measurement functions, J. Adv. Model. Earth Syst., 7, 50–66, doi:10.1002/2014MS000373, 2015.

Skamarock, W. C., Klemp, J. B., Dudhia, J., Gill, D. O., Barker, D. M., Duda, M. G., Wang, X.-Y., Wang, W., and Power, J. G.: A Description of the Advanced Research WRF Version 3 (No. NCAR/TN-475+STR). University Corporation for Atmospheric Research, doi:10.5065/D68S4MVH, 2008.

Vidot, J. and Borbás, É.: Land surface VIS/NIR BRDF atlas for RTTOV-11: model and validation against SEVIRI land SAF
575   albedo product, Q. J. R. Meteorol. Soc., 140, 2186-2196, doi:10.1002/qj.2288, 2014.

Vidot, J., Brunel, P., Dumont, M., Carmagnola, C., and Hocking J.: The VIS/NIR Land and Snow BRDF Atlas for RTTOV:
        Comparison between MODIS MCD43C1 C5 and C6, Remote Sens., 10(1), 21, doi:10.3390/rs10010021, 2018.

Vukicevic, T., Greenwald, T., Zupanski, M., Zupanski, D., Vondar Harr, T., and Jones, A. S.: Mesoscale cloud state estimation
        from visible and infrared satellite radiance. Mon. Wea. Rev., 132(12): 3066-3077. doi:10.1175/MWR2837.1, 2004.

580 Várnai T. and Marshak A.: Statistical Analysis of the Uncertainties in Cloud Optical Depth Retrievals Caused by Three-
        Dimensional   Radiative   Effects,   J.   Atmos.   Sci.,   58(12),   1540-1548,   doi:10.1175/1520-
        0469(2001)058<1540:SAOTUI>2.0.CO;2, 2001.

Xue, J. S.: Scientific issues and perspective of assimilation of meteorological satellite data, Acta Meteorol. Sin., 67(9), 903-
        911, 2009, https://doi.org/10.3321/j.issn:0577-6619.2009.06.001, 2009 (in Chinese with English abstract).

585 Yang, C., Liu, Z., Bresch, J., Rizvi, S. R. H., Huang, X.-Y., and Min, J.: AMSR2 all-sky radiance assimilation and its impact
        on the analysis and forecast of Hurricane Sandy with a limited-area data assimilation system, Tellus A: Dynamic
        Meteorology and Oceanography, 68:1, 30917, doi:10.3402/tellusa.v68.30917, 2016.

Yang, J., Zhang, Z., Wei, C., Lu, F., and Guo, Q.: Introducing the New Generation of Chinese Geostationary Weather Satellites,
        Fengyun-4, B. Am. Meteorol. Soc., 98(8), 1737-1658, doi:10.1175/BAMS-D-16-0065.1, 2017.

590 Zhang, A. and Fu. Y.: Life Cycle Effects on the Vertical Structure of Precipitation in East China Measured by Himawari-8
        and GPM DPR, Mon. Wea. Rev., 146(7), 2183–2199, doi:10.1175/MWR-D-18-0085.1, 2018.

Zhang, M., Zupanski, M., Kim, M.-J., and Knaff, J. A.: Assimilating AMSU-A Radiances in the TC Core Area with NOAA
        Operational HWRF (2011) and a Hybrid Data Assimilation System: Danielle (2010), Mon. Wea. Rev., 141(11), 3889-
        2907, doi:10.1175/MWR-D-12-00340.1, 2013.

595 Zhang, P., Zhu, L., Tang, S., Gao, L., Chen, L., Zheng, W., Han, X., Chen, J., and Shao, J.: General Comparison of FY-
        4A/AGRI With Other GEO/LEO Instruments and Its Potential and Challenges in Non-meteorological Applications, Front.
        Earth Sci., 6, 224, doi:10.3389/feart.2018.00224, 2019.

Zhou, Y. Liu, Y., Huo, Z., and Li, Y.: WRF-DART/RTTOV input and (processed) output files for GMD-2022-30, Zenodo,
        doi: 10.5281/zenodo.6417682 , 2022.

600 Zhou, Y., Liu, Y., and Liu, C.: A machine learning-based method to account for 3D Short-Wave radiative effects in 1D satellite
        observation operators, J. Quant. Spectrosc. Radiat. Transf., 275, 107891, doi:10.1016/j.jqsrt.2021.107891, 2021.